Supplementary information

Pyroelectric effects inducing negative feedback boiling heat transfer

Miaoxin Ma [a], Hui He *[a], Xiang Chai [a], Tengfei Zhang [a], Jinbiao Xiong [a], Xiaojing Liu *[a]

a School of Nuclear Science and Engineering, School of Mechanical Engineering, Shanghai Jiao Tong University, Shanghai 200240, China

* Corresponding author, E-mail: ME_hehui@sjtu.edu.cn & xiaojingliu@sjtu.edu.cn

Supplementary Note 1: Experiment and simulation methods

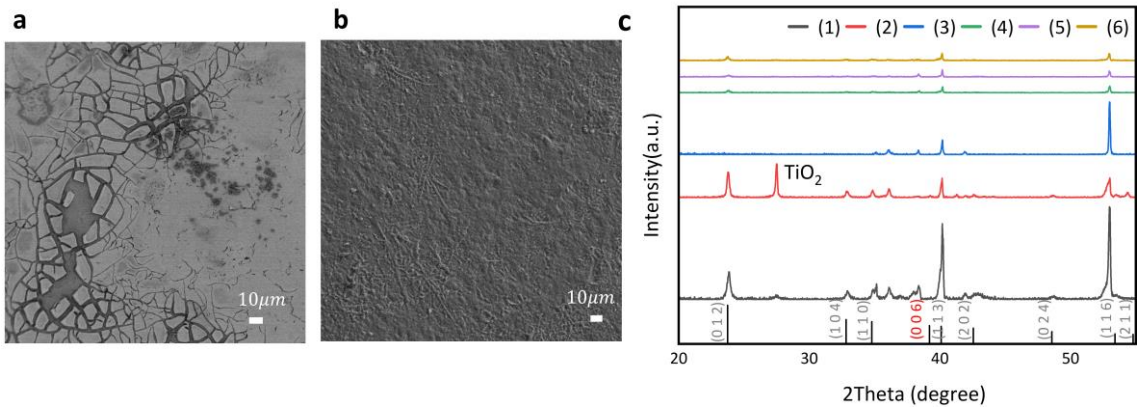

Fig. S1 (a) SEM image of Ti substrate; (b) SEM image of Ti-Pt substrate; (c) XRD images of the six different surfaces (1-6): (1) annealing temperature of 923 K, curing time of 15 minutes, and 24-hour sol settling time; (2) annealing temperature of 923 K, curing time of 15 minutes, and 48-hour sol settling time; (3) annealing temperature of 973 K, curing time of 15 minutes, and 48-hour sol settling time; (4) annealing temperature of 973 K, curing time of 10 minutes, and 72-hour sol settling time; (5) annealing temperature of 973 K, curing time of 15 minutes, and 72-hour sol settling time; (6) annealing temperature of 973 K, curing time of 20 minutes, and 72-hour sol settling time

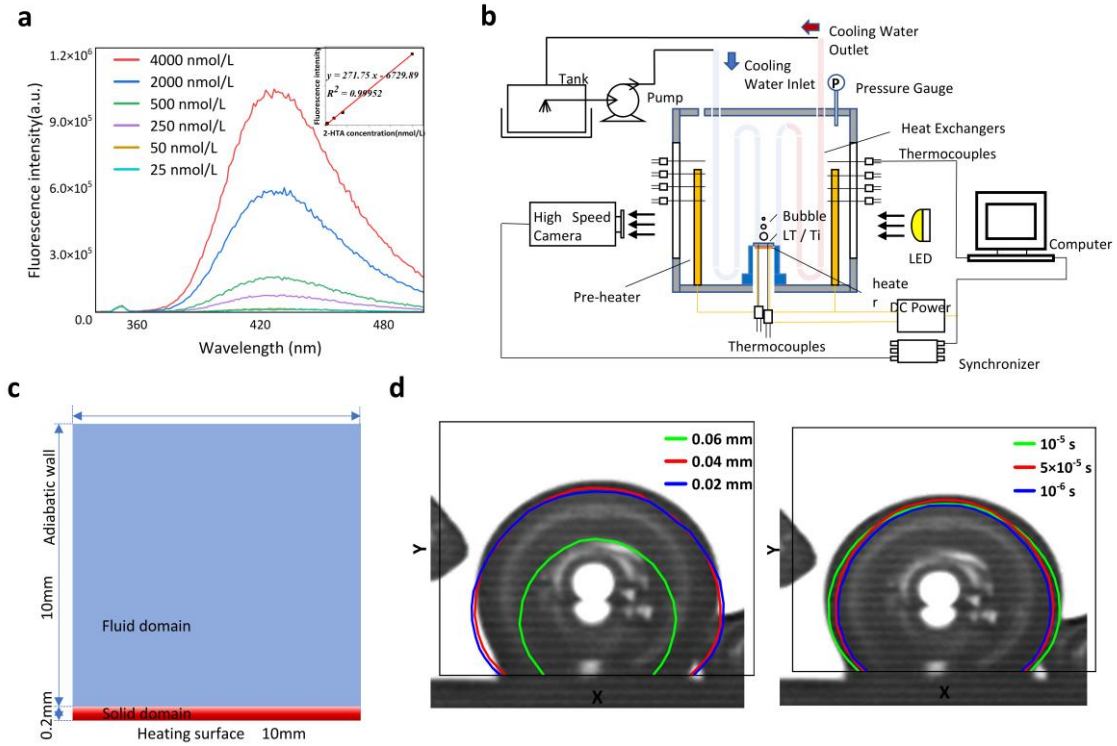

Fig. S2 (a) Fluorescence spectra of different concentrations of HTA solutions; (b) Schematic of the pool boiling experimental system; (c) Schematic of computational domain; (d) Grid-independent verification and comparison of bubble shape and size in the experiment with the simulation.

Synthesis of lithium tantalate and performance characterization methods

The sol-gel method[1] is an important technique for fabricating thin coatings. This method involves the synthesis of sol from precursor materials and subsequent gelation to form a solid network. By carefully controlling the sol-gel parameters, such as precursor concentration, pH, and temperature, it is possible to achieve thin coatings with desired properties. This method has several advantages, including the ability to control the stoichiometry of tantalum and lithium in the coating, lower production and equipment costs, and suitability for large-area coating formation. Thus, LT is prepared by sol-gel method and its possibility of reversible transition in wettability is explored. The synthesis of LT involves the following steps: Anhydrous lithium acetate (CH_3COOLi, 98%) is dissolved in 1,2-propanediol ($C_3H_8O_2$, 98%) at a 1:10 ratio. This mixture is then heated to 383 K in an oil bath, with continuous stirring at 100 rpm for 3 hours, ensuring the complete dissolution of the lithium acetate. After heating, the mixture is cooled to 313 K. Subsequently, butyric acid ($C_4H_8O_2$, $\geq$99.8%) is added while stirring continuously to adjust the pH to between 5 and 6. An equivalent molar amount of ethanol tantalum ($C_{10}H_{25}O_5Ta$, 98%) is then introduced to maintain a 1:1 molar ratio of Li^+: Ta^{5+}. The mixture undergoes reflux at 403 K for 72 hours, enabling sufficient condensation reactions between Ta^{5+} and Li^+ to form stable Li-O-Ta bonds. This process yields a steady brownish-yellow LT solution with a concentration of 0.5 mol/L.

Fig. S1 (a) and (b) are scanning electron microscope (SEM) images of the Ti substrate and Ti-Pt substrate, respectively. The Ti substrate shows visible cracks and particle accumulation, indicating poor coating quality. This is due to the mismatch in the coefficient of thermal expansion between the coating and the Ti substrate, leading to stress accumulation and cracking during high-temperature annealing. The particle accumulation is attributed to impurities or incomplete coating formation. On the other hand, the Ti-Pt substrate shows a flat and uniform coating with improved crystalline properties. This can be attributed to the use of Pt as a transition layer, which provides a better match in the coefficient of thermal expansion with the coating material. The Pt layer acts as a buffer, reducing the stress accumulation and improving the coating quality. Therefore, LT is the optimal choice for achieving high-quality coatings suitable for our experimental objectives, given that its thermal expansion coefficient closely matches that of the Pt transition layer. Consequently, all characterisations of coating structure, pyroelectric performance measurements and pool boiling experiments described in the study are conducted on LT surfaces prepared on Ti-Pt substrates, with smooth Ti surfaces serving as control groups.

The substrate synthesis consisted of first sandpapering titanium (Ti, ≥99.5%) followed by ultrasonic cleaning in acetone (C_3H_6O, ≥99.5%), anhydrous ethanol (CH_3CH_2OH, ≥99.8%), and deionized water, sequentially. The platinum (Pt) layer is then coated as a transition layer using a high-vacuum sputtering instrument, the Q 150T ES plus, with a sputtering time of 15 seconds, resulting in a thickness of approximately 10 nm. During spin coating, the Ti-Pt substrate is placed on the spin coating table and secured using a vacuum pump. The LT colloidal solution then evenly spreads over the substrate under the following conditions: 500 rpm for 15 seconds, followed by 3000 rpm for 60 seconds. After spin-coating, the wet coating is immediately cured in a muffle furnace at 393 K. The LT is then subjected to thermal annealing in a tube furnace, the annealing atmosphere is air, and pressure conditions are atmospheric. This process is divided into three stages: firstly, heating to 523 K for 10 minutes to decompose and volatilize organic components; secondly, increasing the temperature to 723 K for 10 minutes to decompose reaction by-products; and finally, raising the temperature to various experimentally determined annealing temperatures for 1 hour to fully crystallize the LT coatings. The heating rate was 0.5 K/s and the cooling rate was -0.5 K/s throughout. After annealing, the samples are taken out and stored under a vacuum.

Phase analysis of the coatings is conducted using X-ray diffraction (XRD), employing the D8 ADVANCE Da Vinci multifunctional X-ray diffractometer. The surface morphology and roughness are characterized using the 3D Laser Scanning Microscope VK-X3000. Further, the prepared LT coating's surface morphology is observed and characterized using the JSM-7800F field emission scanning electron microscope (SEM) and the high-throughput scanning electron microscope, which is equipped with a secondary electron detector, offering a resolution of 1.5 nm. The SEM captures images with a pixel dimension of 2048×2048 and a pixel size of 0.7 nm, enabling the detailed visualization necessary for

accurate nanoparticle size measurement. Particle size measurements are conducted using ImageJ, and the data is statistically analyzed using Origin.

To further analyse the pyroelectric properties of the coatings, the XRD image of the six different coatings is presented in Fig. S1 (c). Due to the pronounced anisotropy of LT, it is required for the LT thin coating to grow along the c-axis direction, i.e., the (006) direction, which possesses the highest pyroelectric coefficient. The six coatings are prepared by adjusting several conditional parameters and XRD patterns reveal distinct differences among the six coatings. The annealing temperature, curing time, and sol settling time all have effects on LT synthesis. The annealing temperature affects the crystal structure as well as the material properties, and a comparison of the coatings (2), (3) shows that the XRD peaks of 923 K are sharp and well-defined, indicating a highly crystalline structure. This suggests that annealing at 923 K is favourable for achieving a more desirable crystal structure, whereas higher temperatures may lead to excessive grain growth or crystal structure disruption. Curing time affects the crystallinity and thermal stability. Comparison of coatings (4), (5), and (6) shows that the XRD pattern of 15 minutes curing time is better than that of 10 and 20 minutes. Too short curing time leads to incomplete formation of the coating, which affects the denseness and stability of the coating, while too long curing time may lead to surface damage, which affects the crystalline quality. The molecules in the sol during the sol settling time undergo a condensation reaction to form a gel with a three-dimensional lattice structure, which directly affects the quality of the coating. A comparison of coatings (1), (2), and (5) shows that the crystalline quality is better at a sol settling time of 24 hours than that of 48 and 72 hours. Too short a settling time may not allow sufficient condensation reaction in the sol, affecting the crystal structure, while too long a settling time may lead to irregular precipitation of the gel structure and generation of impurities, affecting the uniformity of the coating and the application effect. Titanium dioxide (TiO_2) is found to appear in the coating, which may be due to the surface cracking and exposure of the Ti substrate at high temperatures, resulting in the reaction between titanium and oxygen to form TiO_2. Overall, coating (1) exhibits the most favourable XRD pattern, indicating the highest crystallinity and preferred growth along the c-axis direction.

The pyroelectric efficiency of the LT coatings is tested using hydroxyl radicals. Pyroelectric materials exhibit changes in polarization intensity and surface charge when the temperature changes. In equation (1), they undergo a chemical reaction with hydroxide ions in water, resulting in the generation of hydroxyl radicals.

$$OH^- + q^+ = \cdot OH \tag{1}$$

To detect the generation of hydroxyl radicals, this study employs terephthalic acid (PTA) as a probe molecule. TA rapidly reacts with hydroxyl radicals through hydroxylation of its aromatic rings, forming 2-hydroxyterephthalic acid (HTA) with high fluorescence characteristics. The fluorescence intensity of the product HTA, which is indicative of hydroxyl

radical concentration, can be measured using a fluorescence spectrometer and is positively correlated with the concentration of hydroxyl radicals. The experiments are carried out based on the property that pyroelectric materials generate charges in cold–hot alternation environments to generate hydroxyl radicals with hydroxide ions in water. Hydroxyl radicals are tested under temperature gradients formed by setting different temperatures in two water baths. Firstly, a 10 ml solution of PTA (1×10^{-3}mol·L^{-1}) is prepared and heated in a beaker to the desired temperature (323 K). At the same time, the sample is placed in the water bath of another temperature. Then, the sample is placed in the PTA solution and reacted for 2 minutes before being transferred to the beaker of the other temperature (293 K). This process is repeated five times. After the temperature cycling, the reaction solution is immediately analyzed using the fluorescence spectrometer FLS1000 at Shanghai Jiao Tong University Instrumental Analysis Center. The excitation wavelength is set at 315 nm, and the emission wavelength is set at 425 nm to measure the fluorescence intensity of HTA. By comparing with the fluorescence intensity of a pre-prepared standard HTA solution, a linear relationship between the fluorescence intensity at 425 nm and the concentration of HTA was established, as shown in Fig. S2 (a). This curve correlates the fluorescence intensity with the apparent concentration of hydroxyl radicals, thereby allowing the assessment of the pyroelectric performance of the LT coating and its potential application in achieving temperature-sensitive self-regulation of wettability. Each experiment is conducted three times to ensure the reproducibility of the results, and the average of these three measurements is taken.

Pool boiling test systems and test methods

Fig. S2 (b) shows the pool boiling experimental system, which comprises a pool boiling chamber, a DC power supply, a temperature control module, a high-speed camera, and a temperature acquisition system. The pool boiling chamber, made of 304 stainless steel, has a total capacity of approximately 5.8 litres (168 mm×168 mm×208 mm). Two tempered glass windows are located on the side walls of the chamber to provide lighting and enable high-speed camera shooting during the experiment. The experiment controls the saturation state of the working fluid by using heating rods and heat exchangers.

The experiments are carried out using the prepared LT surfaces (20 mm×20 mm×2mm) with a smooth Ti surface used as a control. The surface is indirectly heated by a polyimide heating coating. Thermocouples are used to obtain the temperature at various locations of the fluid on the side panels of the pool boiling chamber. The temperature of the sample is obtained by thermocouples welded to the bottom of the sample. The error of the thermocouple is ±0.5 ℃. The experimental system's temperature is recorded by a data acquisition recorder connected to a computer. The parameters of the DC power supply are adjusted to achieve different wall superheat and transient heating/cooling rates. Additionally,

a high-speed camera is also used to record the bubble behaviours on the surface, which is captured at a resolution of 1280×1024 and a frame rate of 1000 FPS. Each experiment is conducted three times to ensure the reproducibility of the results, and the average of these three measurements is taken.

The experiments are conducted at atmospheric pressure corresponding to a saturation temperature of 373 K, maintaining the LT in its ferroelectric state while avoiding the complexities associated with high-pressure experiments. High-pressure conditions, such as 15 MPa, which correspond to a saturation temperature above 613 K, would necessitate advanced experimental equipment and make visualization challenging due to the low surface tension and propensity for bubble coalescence at elevated temperatures.

The wettability of the surface can be characterized by the contact angle, while the rate of temperature change on the sample surface is achieved by quickly adjusting the electric power of the heating element. The visualized images of the bubble formation process are captured by a high-speed camera. Each image is timestamped, thus allowing for precise location of the time for each image. The bubble life cycle consists of three distinct stages: nucleation, which signifies the commencement of bubble formation; growth, during which the bubble expands on the heated surface; and detachment, the point at which the bubble separates from the heated surface. To maintain uniformity in the contact angle data, a specific stage within the bubble life cycle has been selected for measurements. The contact angle is measured when the bubble attains its maximum diameter during the growth phase, as this phase presents a more stable bubble shape compared to the initial and final stages of growth. At this juncture, the effect of temperature changes on wettability is most pronounced. During the growth of bubbles in pool boiling, bubbles at the same location after temperature change are visually recorded, and then the values of their advancing and receding contact angles are calculated and averaged by image processing and algorithms. The ImageJ software is utilized to standardize the measurement process, reducing human error, with the capability to enhance accuracy for smaller particles through localized zooming. The contact angle data obtained at the same stage within different bubble life cycles is analysed to investigate the variation of the wettability of the surface under temperature change. This part of the experiment records the unsteady state of the temperature change process, and the curves of the surface contact angles of Ti and LT as a function of time for different temperature change rates are obtained. The difference in temperature change for different operating conditions is evaluated in terms of the temperature change rate r. The heating condition is to apply power from the point ONB, which causes the surface temperature to change rapidly. The cooling condition is the withdrawal of the newly applied electric power to bring the surface back to the ONB point after the completion of the corresponding heating condition.

The boiling curve is determined by pool boiling experiments, and the relationship between heat flux and wall superheat of Ti and LT is measured. The boiling curves have labels showing the errors of wall superheat and heat flux for

each data point. The error of wall superheat comes from the high-frequency measurement of the thermocouple within 2s. The thermocouple reading frequency is 10 Hz, and the average temperature within 2s is considered the current temperature in the experiments. The error of the heat flux comes from the fluctuation of the power supply oscillations. The output current in the power supply is constant in the C-V mode, with the voltage fluctuating slightly. The actual power is determined by averaging three consecutive 2-second measurements. The thermal flux density is determined by the ratio of the actual power of the heating element to the contact area and the error coefficient N, as shown in Equation (2). The actual power is obtained by multiplying the voltage and current of the direct current power supply. The contact area is 20×20 mm². The error coefficient takes into account the thermal losses of the entire process, which is measured in advance before the experiment, and since the overall temperature rise range is small, it is considered constant, with a value of 1.5. The temperature value T_1 is the reading from the thermocouple at a depth d_1 of 0.7 mm, with d being the total thickness of the sample. The wall temperature is calculated using Equation (3). The fluid temperature T_f near the sample is obtained from a thermocouple above the sample. The wall superheat ΔT is given by Equation (4), where λ is the thermal conductivity of the material. The surface HTC can be calculated by evaluating the surface heat flux and temperature data using Equation (5). The error in the surface HTC is determined by the error transfer function from the heat flux q and wall superheat ΔT, as given by Equation (6).

$$q = UI / AN \tag{2}$$

$$T_w = T_1 - q(d - d_1) / \lambda \tag{3}$$

$$\Delta T = T_w - T_f \tag{4}$$

$$HTC = q / (T_w - T_f) = q / \Delta T \tag{5}$$

$$\sigma_{HTC} = HTC \cdot \sqrt{\left(\frac{\sigma_q}{q}\right)^2 + \left(\frac{\sigma_{\Delta T}}{\Delta T}\right)^2} \tag{6}$$

Numerical simulation setup

Geometrical modeling

Fig. S2 (c) shows the division of the computational region and boundary conditions in the numerical simulation. The computational domain is divided into two parts: the solid domain and the fluid domain. The solid domain simulates coupled fluid-solid heat transfer, while the fluid domain simulates vapor-liquid interface heat and mass transfer. The computational domain has pressure exit conditions, with a vapor reflux volume fraction of 0 at standard atmospheric pressure. For the experiment on saturated boiling, the initial fluid temperature in the fluid domain is 373 K, and the heat

flux is added to the heating surface. A quadrilateral mesh with high precision is used for mesh delimitation, and the grid orthogonal mass is 1, which is the best orthogonal mass.

VOF model

The bubble growth process of boiling heat transfer in the VOF model[3,4] is vapor-liquid incompatible with each other, the mass is conserved in the fluid domain, and the continuity equations are Equations (7) and (8):

$$\frac{\partial \alpha_v}{\partial t}+\frac{\partial(\alpha_v u)}{\partial x}+\frac{\partial(\alpha_v v)}{\partial y}=\frac{M_v}{\rho_v} \tag{7}$$

$$\frac{\partial \alpha_l}{\partial t}+\frac{\partial(\alpha_l u)}{\partial x}+\frac{\partial(\alpha_l v)}{\partial y}=\frac{M_l}{\rho_l} \tag{8}$$

where α is the volume share, ρ is the density, and M_v and M_l are the vapor and liquid mass source terms. The momentum is conserved in the computational domain and the obtained velocity field is shared between the vapor and liquid phases, and the solved energy and momentum equations are Equations (9) and (10):

$$\frac{\partial}{\partial t}(\rho cT)+\nabla\cdot\left(u\cdot\rho cT\right)=\nabla\cdot\left(\lambda\cdot\nabla T\right)+h \tag{9}$$

$$\frac{\partial}{\partial t}(\rho\vec{u})+\nabla\cdot\left(\rho\vec{u}\vec{u}\right)=-\nabla p+\nabla\cdot\left(\mu\cdot\nabla u\right)+F_x+F_g \tag{10}$$

where c is the specific heat at constant pressure, λ is the thermal conductivity, μ is the kinematic viscosity coefficient, h is the energy source term, F_g is the gravity, and F_x is the liquid mass source term for surface tension.

Surface tension model

The changes in the vapor-liquid interface during bubble generation and growth are captured to illustrate the heat transfer mechanism with varying surface wettability. Since the vapor-liquid interface is a high-curvature interface and is constantly changing, the CSF continuous surface tension model is chosen[5]. The CSF model can convert the surface tension of the high curvature of the vapor-liquid interface into a volumetric force that is added to the momentum equation, and the corresponding surface tension equation is given by Equation (11):

$$\begin{cases} F_x=\dfrac{\sigma\left(\alpha_l\rho_l\kappa_l+\alpha_v\rho_v\kappa_v\right)}{0.5(\rho_l+\rho_v)} \\ \kappa=\nabla\cdot\hat{n} \\ \hat{n}=n/|n| \\ n=\nabla\alpha_\kappa \end{cases} \tag{11}$$

where σ is the surface tension coefficient, and the surface tension coefficient of water at 0~100℃ is a temperature-dependent variable. $\hat{n}$ is the unit surface normal vector estimated by the volume fraction gradient; κ is the local surface curvature, the vapor-phase interfacial curvature and liquid-phase interfacial curvature are opposite to each other for two-phase substances.

Heat and mass transfer model

Water and vapor are immiscible with each other during bubble growth. In the numerical simulation, the heat and mass transfer that occurs at the vapor-liquid interface is modelled using the mass transformation model[6]. When the temperature of the computational grid near the interface is greater than the saturation temperature, the liquid-phase mass begins to transfer to the vapor-phase, and the bubbles gradually grow, and vice versa as indicated by Equations (12) and (13):

$$T > T_{sat}, M_{l\to v} = c_l \alpha_l \rho_l \frac{T - T_{sat}}{T_{sat}} \tag{12}$$

$$T < T_{sat}, M_{v\to l} = c_v \alpha_v \rho_v \frac{T - T_{sat}}{T_{sat}} \tag{13}$$

Add $M_{l\to v}$ to Equation (7) to calculate the mass of the phase change in the liquid phase; $M_{v\to l}$ to Equation (8) to calculate the mass of the phase change in the vapor phase. c_l and c_v are the relaxation factors of the phase change; the mass is conserved within the grid during the process of boiling heat transfer, the evaporation of the vapor phase is equal to the amount of condensation of the liquid phase, and the evaporation and condensation relaxation factors are equal, and the size of the value needs to be adjusted according to the results of the experiments. When the phase transition occurs, the mass source term is multiplied by the latent heat of the phase transition to obtain the energy source term.

Equations (7)-(10) are solved numerically using the finite volume method. The spatial derivatives in the momentum and energy equations are discretized using the second-order implicit, and the time derivatives are discretized using the first-order implicit to increase the solution accuracy. The pressure-velocity coupling in the momentum equation is corrected for neighbourhood and skewness with the pressure implicit in the operator splitting algorithm (Piso), and the pressure staggering option (PRESTO!) is used to deal with the high curvature problem that occurs at the vapor-liquid interface.

Model verification

The verifications of grid-independence and time-independence are conducted on the fluid domain, as shown in Fig. S2 (d). Grid resolutions of 0.06mm, 0.04mm, and 0.02mm are tested to investigate the effect of grid size on simulation results. The results indicate that there is no significant difference between grid sizes of 0.04mm and 0.02mm. Therefore, a grid size of 0.04mm with 66,515 grids is chosen. The time-independence verification is then carried out using time steps of 10^{-5} s, 5×10^{-6} s, and 10^{-6} s. For each time step, the convergence criterion for the normalized residual sums of mass, momentum, and velocity is fixed at 10^{-3}, and that for the normalized residual sums of the energy equations is fixed at 10^{-6}, which satisfies the Friedrichs-Lewy constraints (LCF). The results show that the results are essentially unchanged at grid sizes of 5×10^{-6} s and 10^{-6} s. Therefore, the time-independent grid size for the computational results is 5×10^{-6} s. Subsequently, the applicability of the simulation is corroborated through a comparison of the simulation results with the

experimental data. Fig. S1 (d) presents a comparison between the experimental and numerically simulated bubble shapes and sizes when boiling at a heat flux of 20 kW/m² under a titanium substrate. In regard to bubble shape, the numerical simulations exhibit comparable characteristics to the experimental results, particularly in terms of growth and detachment. Additionally, the maximum lateral length and height dimensions of the numerically simulated bubbles align more closely with the experimental bubble profile dimensions. This suggests that the numerical model is capable of simulating the experiment with greater fidelity, thereby establishing a foundation for further simulations.

Supplementary Note 2: Characterization of lithium tantalate

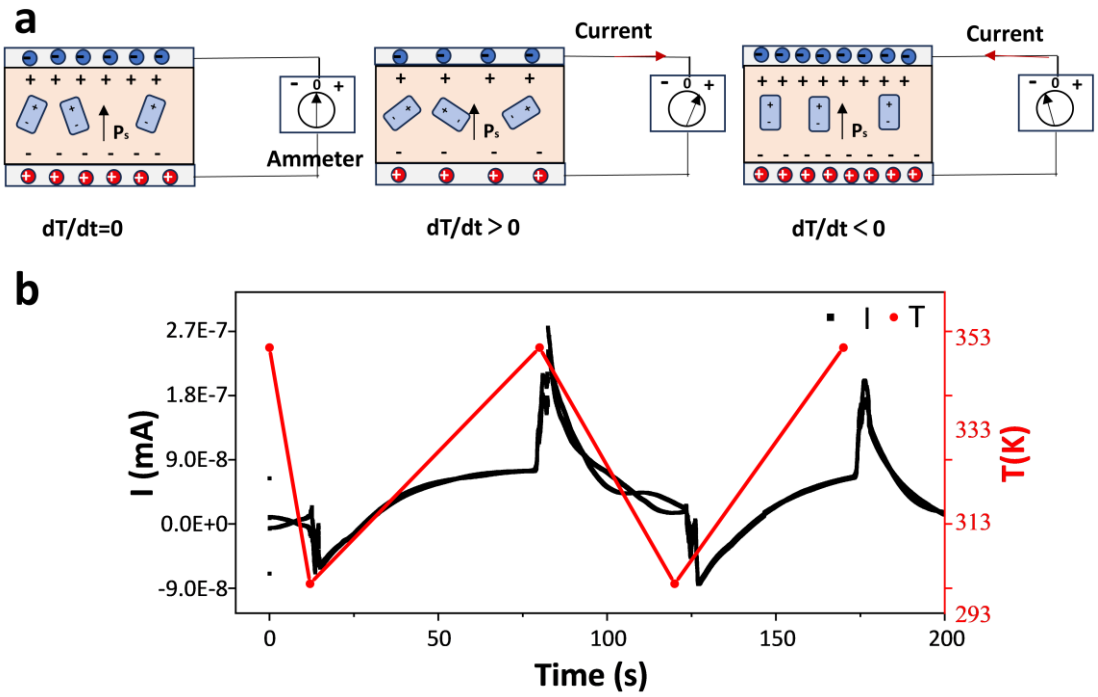

Fig. S3 (a) Schematic diagram of the pyroelectric effect; (b) Temperature T and current I profiles under cyclic fluctuations in temperature.

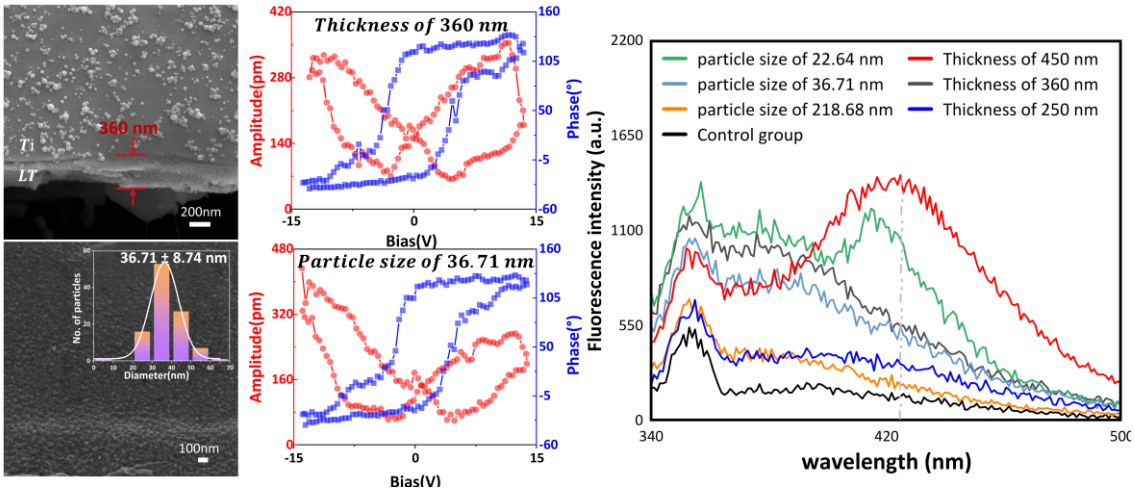

Fig. S4 Comparison of SEM images and ferroelectric switching curves for two coatings and fluorescence spectra of TA solutions with seven different coatings at the same temperature change.

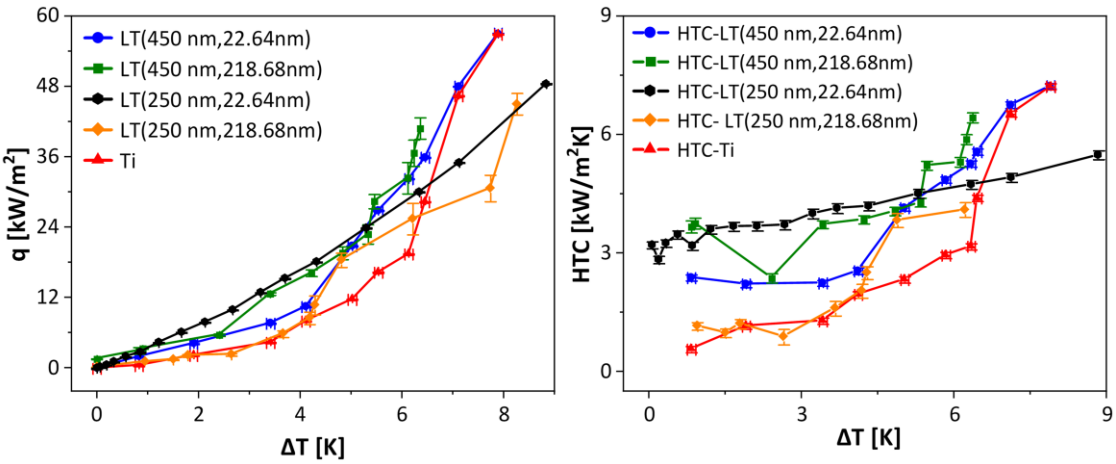

Fig. S5 Boiling and HTC curves for Ti and LT of different sizes.

Lithium tantalate belongs to the trigonal crystal system and exhibits a transition from a cis-electric phase to a ferroelectric phase near its Curie temperature at 878 K. Below this temperature, the crystal enters a ferroelectric state. In the ferroelectric state, the migration of Ta and Li ions along the c-axis leads to the orientation of the dipole moment along this axis. This spontaneous polarization state is temperature-sensitive and varies with thermal conditions, which is the principle of the pyroelectric effect. When the temperature is above the Curie temperature, lithium tantalate crystals exhibit a cis-electric phase, where the positions of Ta and Li ions do not migrate, and no spontaneous polarization occurs, meaning there is no manifestation of the pyroelectric effect.

The pyroelectric effect in the ferroelectric phase is closely related to the polarization direction of the crystal. The polarization direction determines the direction of charge generation under temperature changes. When the polarization direction is consistent with the direction of temperature change, the temperature change will promote further alignment of the electric dipole moments, enhancing the pyroelectric effect, and leading to the production of significant surface charge. If the directions are not consistent, the temperature change may hinder the alignment of the electric dipole moments or even cause them to realign, thereby weakening or offsetting the pyroelectric effect.

To demonstrate the changes in surface charge of lithium tantalate coatings during heating or cooling, as shown in Fig. S3 (a), we have supplemented the verification of charge changes with a dynamic method. Due to the difficulty in distinguishing the true pyroelectric current from any superimposed drift or thermally stimulated currents not originating from pyroelectricity, periodic oscillation of temperature can separate the true pyroelectric current to improve measurement accuracy. This is because the pyroelectric effect is a reversible process; the pyroelectric current generated by heating should be equal in magnitude and opposite in sign to the current generated by cooling at the same temperature change rate. The dynamic temperature is achieved through the rapid potential pulse method of the

electrochemical workstation, which can produce cyclic on-off voltage for the polyimide heating film, thus achieving periodic temperature oscillation. At the same time, the current generated under the periodic oscillating temperature is measured on the second channel of the electrochemical workstation. The specific method involves connecting the top and bottom surfaces of the coating to the working electrode and reference electrode of the electrochemical workstation, respectively, and measuring the current using "zero resistance amperometry," allowing the instrument to measure currents at the pA level.

The correlation curve between temperature T and current I in the supplementary experimental results shown in Fig. S3 (b) indicates that when the temperature decreases, a negative current is generated on the surface of lithium tantalate, with the absolute value of this current increasing over time, indicating the production of negative charges. Conversely, when the temperature increases, a positive current is generated on the surface of lithium tantalate, causing the current curve to gradually increase in the positive direction, indicating the production of positive charges.

The pyroelectric effect, which leads to spontaneous polarization under temperature changes, regulates the distribution of surface charges. Upon temperature increase, the positive charges generated on the surface combine with hydroxide ions in water to form hydroxyl radicals (·OH). Hydroxyl radicals, due to their high reactivity, are generally considered hydrophilic as they can react with water molecules or other polar molecules. When the temperature decreases, the negative charges on the surface react with oxygen in water to form superoxide radicals ($\cdot O_2^-$). Since $\cdot O_2^-$ is relatively stable and less likely to form hydrogen bonds with water molecules, it exhibits hydrophobic properties. This interaction is the basis for the temperature-dependent wettability changes observed on the surface of lithium tantalate.

It has been shown that both piezoelectric and pyroelectric potentials increase with decreasing nanocrystal size or increasing shape factor. The following are the main theoretical descriptions and formulas related to particle size and pyroelectric effects[7]:

The piezoelectric coefficient of nanowires and nanotubes is determined by their size and shape, as shown in the equation:

$$e_{33}\left(D,\lambda\right)=e_{33}\left(\infty\right)+4\lambda e_{33}{}^{S}/D \tag{14}$$

where $e_{33}\left(D,\lambda\right)$ is the piezoelectric coefficient of the nanocrystals, $e_{33}\left(\infty\right)$ is the bulk value, $e_{33}{}^{S}$ is the surface piezoelectric coefficient. D is the characteristic size of the nanocrystals, and λ is the shape factor.

The pyroelectric coefficient of nanocrystals can be approximated by the following expression:

$$p\approx\left(\frac{\partial P_S}{\partial\zeta}\right)_T\left(\frac{\partial\zeta}{\partial T}\right)=e_{33}\alpha \tag{15}$$

where p is the pyroelectric coefficient, P_S is the spontaneous polarization, and α is the thermal expansion coefficient.

The pyroelectric potential can be calculated using the equation:

$$V_{pyro} = \varphi(L) = \frac{pL\Delta T}{\kappa_{33} k_0} \tag{16}$$

where V_{pyro} is the pyroelectric potential, ΔT is the temperature change, *L* is the length of the nanocrystals, and k_0 is the vacuum permittivity.

The theory highlights that both piezoelectric and pyroelectric properties can be significantly enhanced by reducing the size or increasing the shape factor of nanowires and nanotubes. These findings provide a theoretical basis for understanding and predicting the piezoelectric and pyroelectric performance of nanostructures.

To better illustrate the size-dependent effects on the pyroelectric properties of LT, additional experiments are conducted, with the outcomes now depicted in Fig. S4. The results are enriched with further data points across a thickness range of 250 nm to 450 nm and a particle size range of 22.64 nm to 218.68 nm. Notably, measurements for a thickness of 360 nm and particle size of 36.71 nm are incorporated, alongside the assessment of their ferroelectric switching curves and pyroelectric performance. The experimental findings, when considered alongside Fig. 2 of the manuscript, reaffirm the relationship between the thickness and particle size of LT coatings and their pyroelectric performance. The data supports the observation that smaller particle sizes yield increased polarization, intensifying the pyroelectric effect, and that thicker coatings display greater polarization, thereby amplifying the pyroelectric response.

To establish a connection between the size-dependent pyroelectric properties and pool boiling performance, additional pool boiling experiments using LT samples of varying sizes are conducted. The samples are fabricated using the identical method as previously described, with modifications to the spin-coating and annealing processes to achieve the targeted variations in thickness (250 nm and 450 nm) and particle size (22.64 nm and 218.68 nm). Comparisons of the boiling curves and HTC curves across LT samples of different sizes in Fig. S5 reveal the influence of size effects on boiling heat transfer. The results demonstrate that the pyroelectric performance of LT samples influences their heat transfer performance, especially by enhancing the HTC at low heat fluxes and improving safety margins at high heat fluxes. The overall trend indicates that the LT surface with a thickness of 450 nm and a particle size of 22.64 nm exhibits superior heat transfer performance compared to the other samples. As shown in Fig. S5, when the thickness is constant, the LT surface with a smaller particle size displays better boiling heat transfer performance, and when the particle size is constant, the LT surface with a larger thickness shows improved boiling heat transfer performance. These observations suggest that augmenting the pyroelectric effect on the LT surface can further enhance heat transfer performance.

Supplementary Note 3: Relationship between roughness, wettability and nucleation

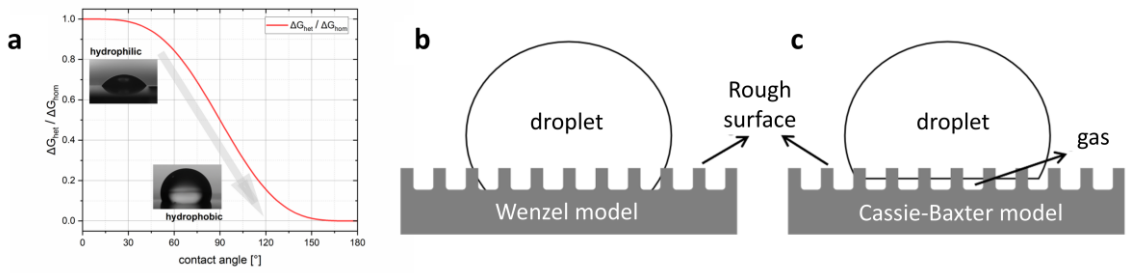

Fig. S6 (a) Variation of critical energy of nucleated surfaces with surface contact angle; (b)Wenzel Model; (c) Cassie-Baxter Model

Classical nucleation theory elucidates the relationship between wetting properties and the nucleation degree during boiling processes, and provides methods for calculating the surface critical energy for heterogeneous nucleation based on the critical energy for homogeneous nucleation.

In classical nucleation theory, the liquid phase fluid on the heat transfer surface must overcome surface tension to initiate the nucleation process, followed by formation and stable growth. The surface critical energy, which represents the minimum energy required for bubble formation, restricts the degree of surface bubble nucleation. In homogeneous nucleation, the surface critical energy depends solely on the thermodynamic properties of the substance, including liquid surface tension and volume-free energy.

Thus, the surface critical energy for homogeneous nucleation is an intrinsic property of a substance, unaffected by external conditions. In heterogeneous nucleation, the surface critical energy is not only related to the thermal properties of the substance, but also influenced by the properties of the material adjacent to the interface, such as surface roughness and chemical properties. Therefore, the surface critical energy for heterogeneous nucleation is influenced not only by the intrinsic properties of the substance itself, but also by the surrounding environment and interface conditions. The relationship given by equations (17) in classical nucleation theory is as follows:

$$\Delta G_{het} = \Delta G_{\hom} cos^4(\frac{\theta}{2})(2-cos\theta) \tag{17}$$

Where ΔG_{het} represents the surface critical energy for heterogeneous nucleation, $\Delta G_{\hom}$ represents the surface critical energy for homogeneous nucleation, and ϑ represents the contact angle of the surface. From the equation, it can be observed that, given a certain surface critical energy for homogeneous nucleation, as the surface contact angle increases, indicating an enhancement in surface hydrophobicity, the nucleation energy barrier of the heat transfer surface decreases, leading to enhanced nucleation. Conversely, a decrease in the surface contact angle reflects an enhancement in surface hydrophilicity. Fig. S6 (a) illustrates the variation of the surface critical energy with the surface contact angle, indicating the dynamic transition of surface wetting properties from hydrophilic to hydrophobic.

The entrainment vapor theory [8] provides a corresponding theoretical model for the more complex and precise bubble nucleation process. This model assumes that the defects on the heat transfer surface are all conical cavities, for fluids with high surface tension. As surface hydrophobicity increases and the surface contact angle enlarges, the fluid fails to wet all the defects on the surface, leading to vapor accumulation within these defects, which then become nucleation sites. The theory presents a relationship for the density of nucleation sites on the heat transfer surface, as given by Equation (18):

$$n = \left(\frac{R_s \Omega(\theta, \varphi) h_{fg} \rho_v}{2 T_{sst} \gamma_{lv}}\right)^m \Delta T^m \tag{18}$$

Where R_S depends solely on the roughness of the heat transfer surface and the dimensions of the conical cavities, Ω is a geometric parameter depending on the contact angle ϑ and the cone angle φ of the nucleation site, h_{fg} and ρ_v represent the latent heat of vaporization and vapor density, T_{sat} is the saturation temperature of the fluid, γ_{lv} is the dynamically changing surface tension, and m is an empirical coefficient determined by the combination of the heat transfer surface and the fluid.

From this relationship, it can be inferred that with smaller nucleation cone angles and larger surface contact angles, the heat transfer surface exhibits a higher density of nucleation sites, indicating superior heat transfer performance. The entrainment vapor theory also elucidates that with larger surface contact angles, the surface boiling intensifies, and the surface hydrophobicity becomes stronger; conversely, surface boiling weakens and hydrophilicity strengthens with reduced surface contact angles.

Surface contact angles are used to characterize the degree of surface wettability. However, another parameter significantly affecting the surface contact angle is surface roughness. This section aims to explore the degree of influence of surface roughness on experimental results. The Wenzel model[9] proposes a method for calculating the uniform surface contact angle of rough protrusions, as shown in Fig. S6 (b). In this model, it is assumed that there is no air at the interface between the solid surface and water, and the rough protrusions on the solid surface are uniformly distributed. Then the contact angle of the rough surface can be described by Equation (19):

$$\cos\theta_r = \frac{A_r}{A}\cos\theta_S \tag{19}$$

Where ϑ_r is the contact angle of the rough surface, ϑs is the contact angle of the smooth surface, A_r represents the actual contact area of the solid surface, and A represents the nominal contact area of the solid surface.

Generally, the rougher the surface, the larger the actual contact area and the diameter of surface conical cavities. As indicated by the Wenzel model, with increasing surface roughness, hydrophilic surfaces become more hydrophilic,

and hydrophobic surfaces become more hydrophobic. For composite materials, the Cassie-Baxter formula[10] is used to calculate the surface contact angle. The Cassie-Baxter model is illustrated in Fig. S6 (c), and the surface contact angle calculation method is described by Equation (20):

$$\cos\theta_n = \frac{A_1}{A_r}\cos\theta_1 + \frac{A_2}{A_r}\cos\theta_2 \tag{20}$$

Where ϑ_n represents the contact angle of the composite rough surface, ϑ_1 and ϑ_2 respectively represent the contact angles of the droplets on the surfaces of two different materials, A_r represents the actual contact area of the solid surface, and A_1 and A_2 respectively represent the contact areas of the liquid with the two materials. The Cassie-Baxter formula can also be used to express the contact angle of non-uniform surfaces. Specifically, if one of the surfaces is in the gas phase, meaning there is solid-liquid contact as well as liquid-gas and solid-gas contact at the interface, then the Cassie-Baxter formula is essentially an extension of the Wenzel model.

In this study, the surface morphology and roughness are characterized using the 3D Laser Scanning Microscope VK-X3000. Meanwhile, to evaluate the range of surface defect scales that can serve as nucleation sites for bubbles, the HSU model was introduced for theoretical calculation[11]. According to the HSU theory, the range of surface defects affecting bubble nucleation is derived from parameters such as wall superheat, fluid temperature, latent heat of vaporization, vapor density, surface tension, and thermal boundary layer thickness. Using these parameters, the theoretical minimum size at 0.1 MPa is estimated to be around 1000 nm.

Supplementary Note 4: Numerical Simulation Analysis of Temperature-Dependent Wettability

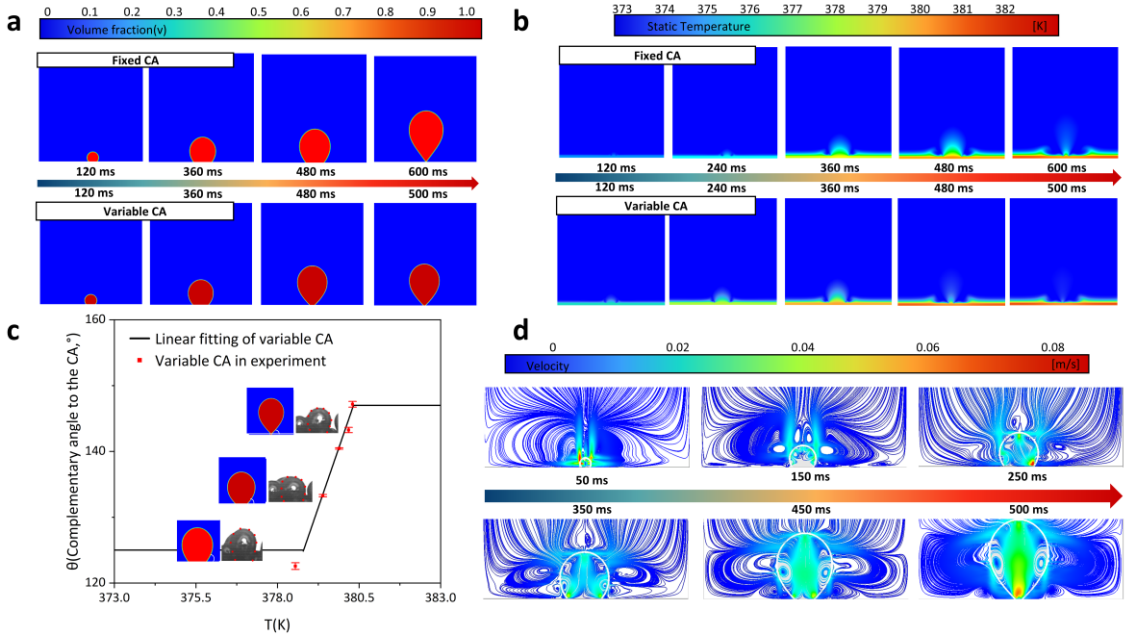

Fig. S7 (a-b) Bubble growth and temperature distribution for two surfaces; (c) Input contact angle in UDF as a function of temperature; (d) Bubble growth and flow field distribution on the surface with various contact angles (In the figure, the abbreviation CA is used to represent contact angle)

As the samples used in this experiment are non-transparent surfaces, revealing the micro-level heat transfer mechanism from the visualization results of the pool boiling experiments is challenging. Therefore, numerical simulations are employed to investigate the micro-level heat transfer mechanism on both the smooth Ti and the LT surfaces. The surfaces are modelled with fixed contact angles and variable contact angles determined through experiments to reflect their unique properties. To delve deeper into the impact of pyroelectric materials on micro-level heat transfer mechanism, the correlation between contact angle and temperature change is established based on bubble behaviour observations, serving as an essential input for the numerical simulations. Based on the fluid-solid coupled heat transfer and VOF model, the relevant UDFs are developed to incorporate energy source terms into the heat and mass transfer model and regulate the wall contact angle based on temperature variations. The UDFs facilitate a qualitative analysis of the coupled boiling heat transfer by pyroelectric materials. The function to modulate the wall contact angle depending on the temperature variation is obtained by linearly fitting the experimental temperature data with the visualization results. As shown in Equation (21), ϑ is the complementary angle to the contact angle of the solid surface θ_c and T_w is the wall temperature. A fixed contact angle of 55° is also set up in the simulation as a control group for the case with temperature-dependent contact angles.

$$\theta=\frac{180^\circ-\theta_c}{180^\circ}\pi,\quad \begin{cases}\theta=\dfrac{25}{36}\pi\ ,\ T_w\le 378.77K\\ \theta=\dfrac{(14.39331T\text{-}5327.18182)\times\pi}{180}\ ,\ 378.77K\le T_w\le 380.34K\\ \theta=\dfrac{147}{180}\pi\ ,\ T_w\ge 380.34K\end{cases} \tag{21}$$

Fig. S7 (c) shows the experimentally obtained varying contact angles of the LT surface at the heating condition of 0.7 K/s and the curve that is linearly fitted and then input into the numerical simulation according to Equation (21). Fig. S7 (a) and (b) show that a single bubble takes 600 ms to grow on the surface with a fixed contact angle and only 500 ms on the surface with variable contact angles under identical conditions. From Fig. S7 (d), it can be seen that the bubble flow field forms vortices only at the top and sides of the bubble when the contact angle changes slightly. However, the image after 350 ms can observe that in addition to the above vortices, a pair of vortices in opposite directions gradually forms on the left and right sides between the bottom of the bubble and the surface, which can carry away the heat near the solid surface and disperse it into the fluid.

References:

1 J. Gou, J. Wang, M. Yang, Z. Huang, W. Li and Y. Jiang, *ACTA METALL SIN*, 2013, **26**, 299–302.

2 F. Tampieri, M.-P. Ginebra and C. Canal, *Anal. Chem.*, 2021, **93**, 3666–3670.

3 L. C. Malan, A. G. Malan, S. Zaleski and P. G. Rousseau, *Journal of Computational Physics*, 2021, **426**, 109920.

4 P. Bhuvankar and S. Dabiri, *Chemical Engineering Science*, 2020, **228**, 115919.

5 K. J. Vachaparambil and K. E. Einarsrud, *Processes*, 2019, **7**, 542.

6 H. Liu, J. Tang, L. Sun, Z. Mo and G. Xie, *International Journal of Heat and Mass Transfer*, 2020, **157**, 119924.

7 H. Jiang, Y. Su, J. Zhu, H. Lu and X. Meng, *Nano Energy*, 2018, **45**, 359–367.

8 V. P. Carey, *Liquid-vapor phase-change phenomena: an introduction to the thermophysics of vaporization and condensation processes in heat transfer equipment*, CRC Press, 2020.

9 R. N. Wenzel, *Industrial & engineering chemistry*, 1936, **28**, 988–994.

10 G. Whyman, E. Bormashenko and T. Stein, *Chemical Physics Letters*, 2008, **450**, 355–359.

11 Y. Y. Hsu, .